Noninvasive MRI-SERS Imaging in Living Mice Using an Innately Bimodal Nanomaterial

Mehmet V. Yigit,[†] Leyun Zhu,[∥] Marytheresa A. Ifediba,[†,‡,§] Yong Zhang,[⊥] Kevin Carr,[∥] Anna Moore,[†] and Zdravka Medarova*[,†]

[†]Molecular Imaging Laboratory, MGH/MIT/HMS Athinoula A. Martinos Center for Biomedical Imaging, Massachusetts General Hospital and Harvard Medical School, Charlestown, Massachusetts 02129, United States, [‡]School of Engineering and Applied Sciences, Harvard University, Cambridge, Massachusetts 02138, United States, [§]Harvard-MIT Division of Health Sciences and Technology (HST) , and [⊥]Center for Materials Science & Engineering, Massachusetts Institute of Technology, Cambridge, Massachusetts 02139, United States, and [∥]Agilton Inc., 15 Cabot Rd, Woburn Massachusetts 01801, United States

ABSTRACT We report a novel nanomaterial (AuMN-DTTC) that can be used as a bimodal contrast agent for *in vivo* magnetic resonance imaging (MRI) and Raman spectroscopy. The probe consists of MRI-active superparamagnetic iron oxide nanoparticles, stably complexed with gold nanostructures. The gold component serves as a substrate for a Raman active dye molecule to generate a surface-enhanced Raman scattering (SERS) effect. The synthesized probe produces T2 weighted contrast and can be used as a SERS active material both *in silico* (in aqueous solution) and *in vivo*. A quantitative assessment of T2 relaxation times was obtained using multiecho MRI analysis. The T2 relaxation times of AuMN-DTTC and MN (dextran-coated iron oxide nanoparticles) were 29.23 + 1.45 and 31.58 + 1.7 ms, respectively. The SERS signature of AuMN-DTTC revealed peaks at 508, 629, 782, 844, 1080, 1108, 1135, and 1242 cm^{-1}. Intramuscular administration of the probe resulted in a decrease of the T2 relaxation time of muscle from 33.4 + 2.5 to 20.3 + 2.2 ms. SERS peaks were observed at 508, 629, 782, 844, 1080, 1108, 1135, and 1242 cm^{-1}, consistent with the *in silico* results. Our studies illustrate for the first time the design and *in vivo* application of a contrast agent, whose component modalities include MRI and SERS. The value of this agent lies in its innately bimodal nature and its application *in vivo* for molecular imaging applications.

KEYWORDS: MRI · SERS · gold nanoparticle · bimodal · Raman · iron oxide nanoparticle · imaging

The recent past has witnessed an increased interest in the development of nanoparticles as contrast agents for biomedical imaging because they have several key advantages over conventional agents. Examples include the potential to envelop nanoparticles with biocompatible polymers,[1] the feasibility of imparting "smart sensing" properties to the probes,[2−5] and the ability to load several other components, including fluorescent tags,[6] drug molecules,[7,8] oligonucleotides,[6,9,10] and peptides,[6] onto the nanoparticles for multimodal and/or multifunctional applications.[11,12] Important prerequisites for the preclinical and clinical applicability of nanoparticles include water solubility, absence of toxic chemicals,[13] capability for functionalization,[14] and the capacity to generate sufficient signal for detection using available medical imaging instrumentation. Recently there has been an interest in developing multimodal approaches because the combination of different modalities into one system compensates for the deficencies of any single imaging modality. Several multimodal probes have been successfully synthesized and characterized,[15−17] including nanomaterials suitable for detection by magnetic resonance imaging (MRI) and photoacoustic imaging,[18] surface plasmon resonance,[19] positron emission tomography (PET),[20] or PET/near-infrared fluorescence (NIRF).[21]

Here we describe the synthesis and application of a novel nanoprobe (AuMN-DTTC), comprised of AuNP complexed with dextran-coated superparamagnetic iron oxide nanoparticles (MN). The agent is synthesized *via* a simple reduction of gold onto the surface of the dextran-coated iron oxide nanoparticles, followed by adsorption of a Raman reporter and PEG chains onto the gold in a process deficient of toxic components.

The dextran-coated iron oxide nanoparticles were selected because of their proven value as preclinical and clinical contrast agents for MRI,[22] whereas our choice of AuNP as a component was prompted by the fact that they have been considered nontoxic,[23] have been used for treatment of certain diseases,[24,25] and have even been applied as CT contrast agents for research purposes.[13,26,27] Due to their easy functionalization *via* thiol-gold chemistry, AuNP have been widely used as biomedical sensors.[9,13,28,29] An additional advantage of AuMN-DTTC is its dual-modality nature.

*Address correspondence to zmedarova@partners.org.

Received for review September 29, 2010 and accepted December 20, 2010

Published online December 31, 2010
10.1021/nn102587h

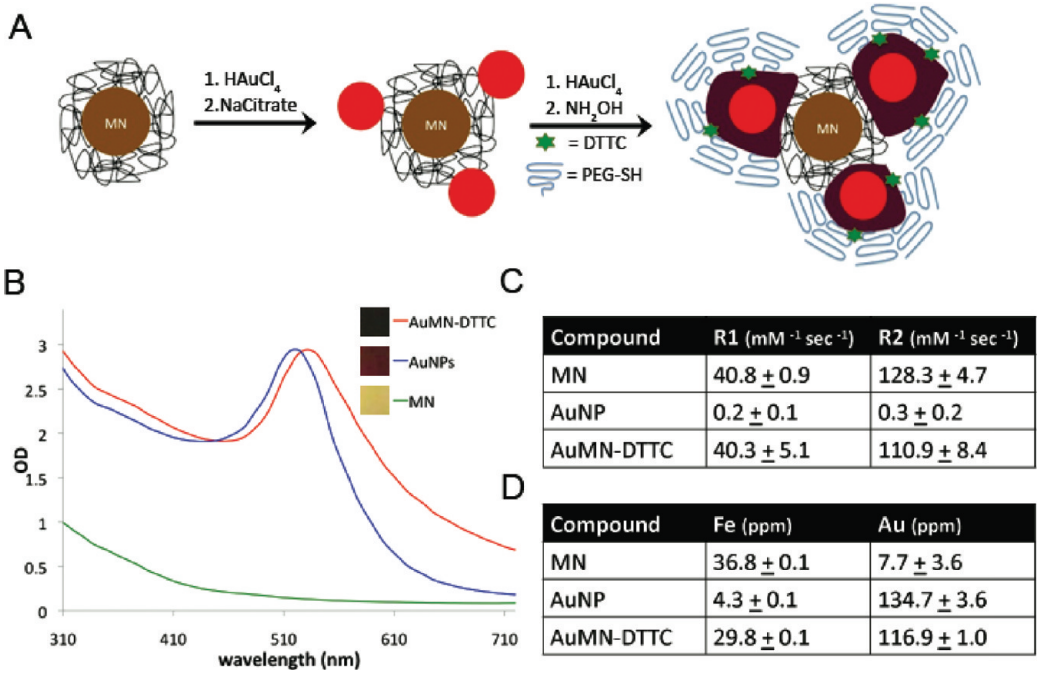

Compound	R1 (mM $^{-1}$ sec $^{-1}$)	R2 (mM $^{-1}$ sec $^{-1}$)
MN	40.8 ± 0.9	128.3 ± 4.7
AuNP	0.2 ± 0.1	0.3 ± 0.2
AuMN-DTTC	40.3 ± 5.1	110.9 ± 8.4

Compound	Fe (ppm)	Au (ppm)
MN	36.8 ± 0.1	7.7 ± 3.6
AuNP	4.3 ± 0.1	134.7 ± 3.6
AuMN-DTTC	29.8 ± 0.1	116.9 ± 1.0

Figure 1. Synthesis and characterization of the MRI-SERS active nanomaterial (AuMN-DTTC). (A) Schematic representation of the synthesis of AuMN-DTTC. The process involves sequential reduction of gold onto the parental MN, expansion of the gold seeds, and incorporation of DTTC and PEG onto the gold seeds. (B) UV absorbance spectra of AuMN-DTTC, AuNP, and MN. The plasmon resonance peak of AuMN-DTTC at 530 nm is an indication of the presence of gold nanostructures in AuMN-DTTC. A digital photograph of the AuMN-DTTC, AuNP, and MN. The deep-red color of AuMN-DTTC is a sign of AuNP in the colloidal mixture. (C) *R*1 and *R*2 values of MN, AuNP, and AuMN-DTTC. The *R*1 and *R*2 values of MN are comparable to those of AuMN-DTTC and significantly higher than those of AuNP ($n = 3$; Student's t test $p = 0.0002$). (D) Elemental analysis of MN, AuNP, and AuMN-DTTC. The experimental AuMN-DTTC probe has iron content comparable to the parental MN and gold content comparable to the parental AuNP.

Iron oxides are contrast agents for MRI,[6,22,30,31] a modality characterized by high spatial and temporal resolution, unlimited tissue penetration, tomographic capabilities, and lack of exposure to ionizing radiation.[32] In addition, our nanoparticles have a gold component that acts to enhance the Raman scattering of reporter dye molecules adsorbed on the nanoparticle surface, transforming them into surface-enhanced Raman spectroscopy (SERS)-active contrast agents.[33−36] The SERS capability is particularly valuable, since it is highly sensitive (two orders of magnitude brighter than quantum dots), and the detailed information gained by this method can readily be distinguished from background tissue signatures.[33,37−39] The advantage of SERS over other modalities lies in its spectroscopic detection and ultrahigh sensitivity suitable for identification of single molecules under certain conditions.[34,40] For instance, in order to obtain an *in vivo* SERS signature, intravenous or intramuscular administration of as little as 50 fmol of SERS active AuNP is enough to obtain a distinguishing SERS spectrum from deep tissues or from tumor xenografts.[36]

Here we demonstrate the suitability of AuMN-DTTC for *in vivo* MRI and Raman spectroscopy. To our knowledge, this is the first report detailing the *in vivo* application of a contrast agent that has MRI and SERS as component modalities and is based on a clinical contrast agent for MRI. By combining the SERS properties of the AuNP and the MRI active properties of AuMN-DTTC, we are able to exploit the properties of both components, resulting in an improvement over existing multimodality technologies and potential relevance in a variety of biomedical applications.

RESULTS AND DISCUSSION

Synthesis and Characterization of the Bimodal AuMN-DTTC Probe. The synthetic scheme of AuMN-DTTC is described in Figure 1A. Briefly, the parental MN was synthesized according to the reported procedure.[6] The gold nanoparticles (AuNP) were doped on MN by reduction of $HAuCl_4$ in the presence of sodium citrate. Following purification, the deposited gold seeds were further enlarged by reduction of $HAuCl_4$ in the presence of hydroxylamine (Figure 1A). A Raman active dye molecule, DTTC, and the stabilizing polymer group, poly(ethylene glycol) (PEG), were later introduced onto the gold surface.[36] The resulting material went through several purification steps to remove free MN and AuNP in the suspension. PEG not only protects the AuNP from degradation and aggregation and ensures a longer circulation half-life but also keeps the Raman active dyes intact on the surface by forming a protective shell around them.[36]

The absorbance spectrum of the probe was monitored by UV−vis spectroscopy and compared with

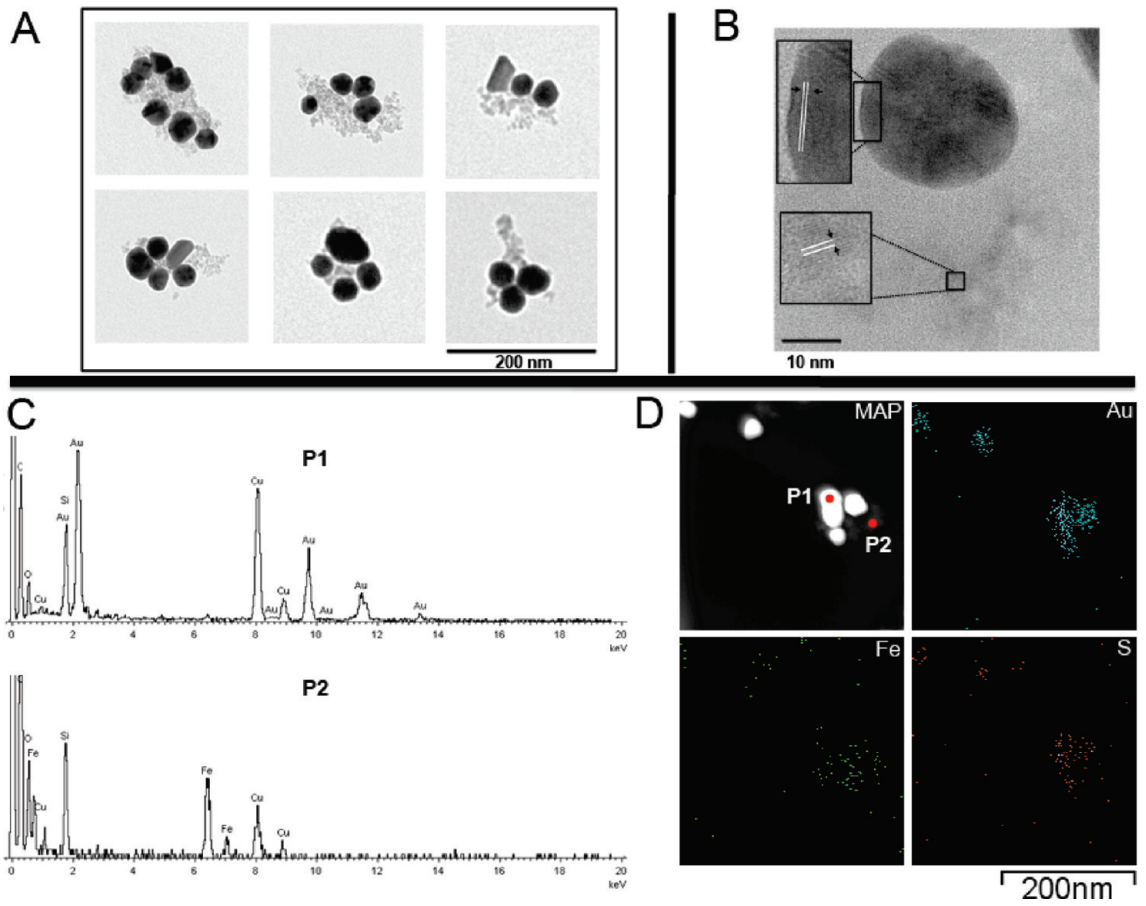

Figure 2. Electron microscopy images of AuMN-DTTC using LWTEM and HRTEM/STEM/EDS. (A) TEM images of AuMN-DTTC suggest that the complex consists of electron-dense AuNP associated with less electron-dense dextran-coated MN. There are several gold nanostructures per probe B) HRTEM images show that the metallic lattices of AuNPs and dextran coated MN are located close to each other. The arrows in the magnified insets show two different metallic lattices. (C) EDS spectra of the dark- and light-colored region in the EDS map show that the nanostructures are composed of gold and iron. (D) Elemental map of the probe. The gold and sulfur components colocalize with the dark-colored region. The iron element colocalizes with the light-colored region of the map and is closely associated with the gold.

AuNP and MN to determine the existence of gold nanostructures in DTTC functionalized gold-doped superparamagnetic iron oxide particles (AuMN-DTTC). As seen in Figure 1B, there is a plasmon peak at 530 nm on the absorbance spectrum of AuMN-DTTC similar to the 520 nm plasmon peak of AuNP, which is a strong indication of the presence of gold nanostructures.[9,13] The absorbance spectrum of MN alone did not have such a feature, indicating that the plasmon peak associated with AuMN-DTTC was due to the presence of gold nanostructures. We also compared the color of the resulting probe, AuMN-DTTC, with AuNP and MN, and we observed that the AuMN-DTTC (0.4 mM Fe, 1.5 mM Au) had a dark-red color, whereas MN (0.4 mM Fe) had a light-brown color[10] and AuNP (1.5 mM Au) had a red color (Figure 1B legend).[9] The red color of the AuMN-DTTC and its absence in MN are a strong indication of the presence of gold in the composition of AuMN-DTTC.[41] We also observed that the darker red color of AuMN-DTTC relative to AuNP is the result of hydroxylamine reduction and enlargement of the AuNP seeds on MN. These results demonstrated the incorporation of gold nanostructures in the resulting probe.

We performed relaxivity measurements on solutions of MN, AuMN-DTTC, and AuNP to determine whether the superparamagnetic feature of MN was preserved in AuMN-DTTC. The $R1$ and $R2$ values of AuMN-DTTC (40.3 ± 5.1 and 110.9 ± 8.4 mM^{-1} sec^{-1}, respectively) were comparable to those of the parental MN probe (Figure 1C).

The elemental analysis of AuMN-DTTC along with the component MN and AuNP was performed to fully quantify the gold and iron content of the final material. Our results indicated that the iron composition of AuMN-DTTC was comparable to the parental MN, whereas the gold content of AuMN-DTTC was similar to AuNP (Figure 1D). These results established that our probe effectively incorporated the iron and gold components.

Since the goal is to apply a given contrast agent *in vivo*, it is important to control the size of the agent within a certain range, given that nanoparticles that are too large are biologically incompatible and nanoparticles

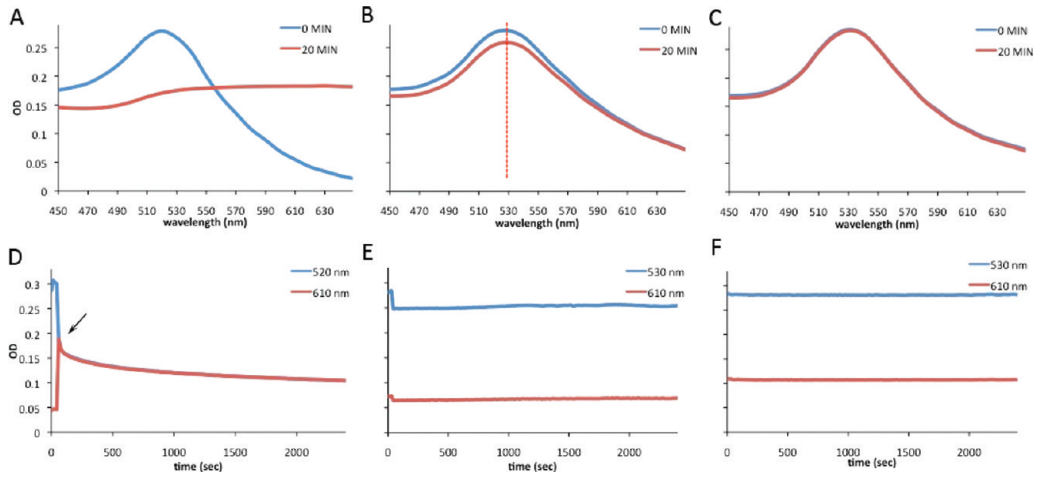

Figure 3. UV−vis absorbance studies of probe stability in FBS or 0.4 M NaCl and 1xPBS. The absorbance spectrum of (A) citrate-stabilized AuNP before and after addition 0.4 M NaCl and 1x PBS, (B) AuMN-DTTC before and after addition of 0.4 M NaCl and 1x PBS, and (C) AuMN-DTTC incubation in fetal bovine serum. Change in absorbance over time of (D) AuNP after the addition of 0.4 M NaCl and 1x PBS (arrow shows the point of addition), (E) AuMN-DTTC after the addition of 0.4 M NaCl and 1x PBS, and (F) AuMN-DTTC in fetal bovine serum. Unlike AuNP, the AuMN-DTTC nanoparticles remained stable long-term both in high-salt conditions and in serum.

that are too small cannot generate sufficient signal for imaging.[13,42] We first analyzed our probes by dynamic light scattering and determined that the average particle sizes of AuMN-DTTC, AuNP, and MN were 94.13 + 1.6, 23.52 + 0.34, and 32.53 + 0.26 nm, respectively (Supporting Information, Figure 1). The zeta potential values for AuMN-DTTC, AuNP, and MN were −2.27 + 0.28, −37.3 + 2.58, and −6.62 + 0.94 mV, respectively.

Several electron microscopy experiments were carried out to obtain structural information about AuMN-DTTC. We first acquired low-resolution transmission electron microscopy (LWTEM) images to determine the overall structure of the probe. As seen in Figure 2A, the gold nanostructures, observed as the electron-dense dark-colored component of the overall probe structure, are complexed with the dextran-coated superparamagnetic iron oxide nanoparticles, the less electron-dense light-colored component in the TEM image. As seen in the figure, there are several AuNP per AuMN-DTTC particles to serve as substrates for SERS.

In order to resolve the structure further we performed high-resolution transmission electron microscopy (HRTEM), scanning transmission microscopy (STEM), and energy dispersive X-ray spectroscopy (EDS) on AuMN-DTTC. As seen in Figure 2B, the dark-colored component (gold nanostructures) of the probe has a metallic lattice that is distinct from the light-colored component (iron oxide nanoparticles). The arrows show the lattices of both gold and iron oxide nanoparticles. This result not only confirms that both components seen in TEM images are metallic nanoparticles but also that they represent different metallic nanostructures (original HRTEM image is provided in Supporting Information, Figure 2).

We focused on the dark- and light-colored region of the probe using STEM/EDS in order to obtain spectroscopic information about the AuMN-DTTC (P1 and P2, Figure 2D map). As seen in the EDS spectra in Figure 2C, the dark-colored component in the structure is indeed composed of gold (P1), whereas the light-colored region is composed of iron (P2). The Cu peak in the spectrum is due to the copper grid used for imaging.

After obtaining the spectroscopic information, we constructed an elemental map on the agent (Figure 2D) to see if the Au, Fe, and S elements are present in the structure and how they are organized spatially with respect to each other. As seen in Figure 2D, PEG is immobilized on gold *via* a thiol bond, as confirmed by colocolization of gold and sulfur in the elemental maps. Also, the iron element colocalizes with the light-colored region of the map and is closely associated with the gold. By contrast an elemental map of sodium ion, a control map, did not detect a distinct spatial signature (Supporting Information, Figure 3). These results along with the results of elemental analysis not only prove that the AuMN-DTTC nanostructures are composed of gold and iron oxide nanoparticles that are complexed with each other but also demonstrate that the gold nanostructures are PEGylated through gold−thiol chemistry.

Stability of AuMN-DTTC in High-Salt Conditions and Serum. After completing the characterization of our probe, we performed a series of experiments to validate the stability of AuMN-DTTC in serum and high-salt conditions relative to citrate-stabilized AuNP. Citrate-stabilized AuNP are stable in water, but in the presence of high-salt conditions, the nanoparticles irreversibly aggregate, resulting in a shift in plasmon resonance.[43] As seen in Figure 3A, the AuNP aggregate after an addition of 0.4 M NaCl and 1xPBS. The aggregation was monitored by changes in optical density at 520 and 610 nm as an indicator of red shift[9,44] over the course of 40 min.

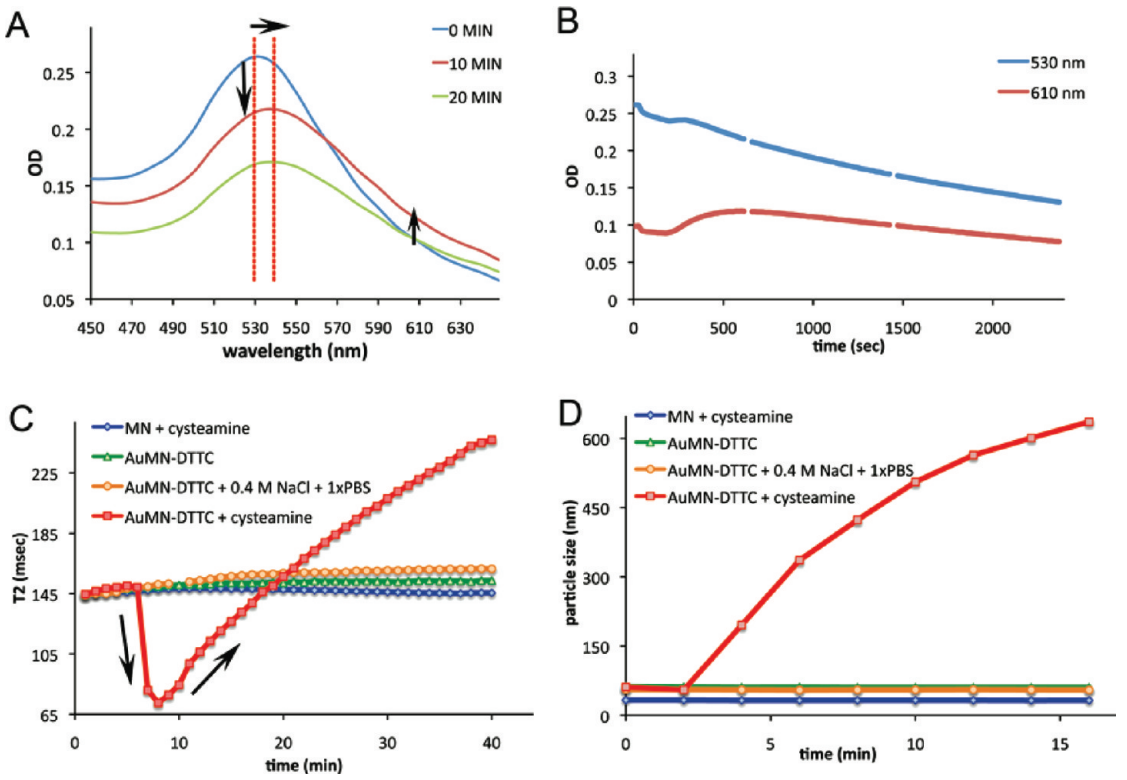

Figure 4. UV−vis absorbance, relaxivity and particle size studies of probe stability in cysteamine and/or 0.4 M NaCl and 1xPBS. Cysteamine induces aggregation of the probe, which can be detected by UV−vis absorbance, relaxivity, and particle size studies. Relaxivity and particle size measurements indicate that treatment with 0.4 M NaCl and 1xPBS does not induce aggregation, confirming the stability of probe. (A) The absorbance spectrum of AuMN-DTTC before and 10 or 20 min after addition of cysteamine. Cysteamine-induced aggregation of the probe is observed as a red-shift of the 530 nm peak. The horizontal arrow shows the red shift at the 530 nm peak. Vertical arrows show the decrease and increase in the 530 and 610 nm reading, respectively. (B) Change in absorbance of AuMN-DTTC over time following the addition of cysteamine. The cysteamine-induced aggregation of the nanoparticles is accompanied by a gradual precipitation of the clusters, visible as a decrease in the 530 and 610 nm peaks. (C) Change in the T2 relaxation time of a solution of AuMN-DTTC in water, 0.4 M NaCl and 1xPBS, or cysteamine. Cysteamine induces aggregation of the probe, visible as a shortening of the T2 relaxation time. Treatment with 0.4 M NaCl and 1xPBS does not produce a similar effect, confirming the stability of probe. Treatment of MN with cysteamine does not result in T2 shortening, due to the absence of the gold component. (D) Particle size change of a solution of AuMN-DTTC in water, 0.4 M NaCl and 1xPBS, or cysteamine. Cysteamine induces aggregation of the probe visible as an increase in nanoparticle size. Treatment with 0.4 M NaCl and 1xPBS does not produce a similar effect, confirming the stability of probe. Treatment of MN with cysteamine does not result in particle aggregation, due to the absence of the gold component.

As seen in Figure 3D, the AuNP aggregate immediately after addition of 0.4 M NaCl and 1xPBS. This is evident from the decrease in the 520 nm peak and the increase of absorbance in the red shoulder due to the aggregation-induced plasmon resonance absorbance shift to longer wavelengths. A further decrease in both the 520 and 610 nm peaks is due to precipitation of the aggregated particles. After developing this approach to monitor the aggregation of AuNP, we performed similar stability measurements of AuMN-DTTC. We first obtained the absorbance spectrum of AuMN-DTTC and observed a 530 nm plasmon peak. After an addition of 0.4 M NaCl and 1xPBS, we did not see a red shift away from the 530 nm peak. However, we observed a slight decrease in OD at 530 and 610 nm, which is due to dilution of the probe with the NaCl/PBS stock solution (Figure 3B). No aggregation was observed over the course of 40 min (Figure 3E), indicating that the AuMN-DTTC preparation had long-term stability in high-salt conditions. In a more biologically relevant context, we measured the absorbance spectrum of our probe (AuMN-DTTC) in fetal bovine serum and did not observe any changes in the 530 and 610 nm peaks over 40 min (Figure 3C and F), suggesting the suitability of AuMN-DTTC for *in vivo* delivery through the circulation. The lack of aggregation in high-salt conditions was also confirmed by assessment of the spin−spin relaxation of the solution, as described below (Figure 4C) and particle size measurements by dynamic light scattering (Figure 4D).

Association of the Gold and Iron Nanostructure Components in AuMN-DTTC. For the purposes of our work, it is important to determine that the MN and gold nanostructures are strongly associated with each other and do not dissociate. To investigate this, we induced aggregation of AuMN-DTTC with a concentrated thiol-containing molecule, cysteamine. At high concentrations cysteamine can replace the PEG molecules on the

gold surface by exchanging the gold−thiol attachment of PEG with that of cysteamine. As the PEG molecules are displaced, the probe is no longer stable and tends to aggregate and finally to precipitate. To promote this, we added a 50 mM solution of cysteamine into the AuMN-DTTC solution. As seen in Figure 4A and B, the 530 nm peak started to decrease and shift to longer wavelengths after the addition of cysteamine, whereas the absorbance over 610 nm increased initially, after which it started to decrease as the aggregated probes precipitated to the bottom of the cuvette. Aggregation is followed by precipitation as the larger clusters of particles cannot stay in suspension, resulting in less absorbent material in the suspension and a corresponding decrease in the 530-nm peak and red shoulder.

The spin−spin relaxation time (T2) values of AuMN-DTTC before and after addition of cysteamine were monitored to demonstrate the stability of the association between the gold and magnetic components of the probe. It has been shown numerous times in the literature that the T2 value of a superparamagnetic nanoparticle solution decreases as the dispersed nanoparticles assemble into clusters. This event has been termed magnetic relaxation switching.[10,45−47] This feature of magnetic nanoparticles has been used to detect different analytes using MRI.[5,47,48] Here, we used this feature of MN to test whether or not the T2 relaxation time of the AuMN-DTTC solution changes as the nanoparticles aggregate. A decrease in T2 relaxation time further confirms that the MN and AuNP are strongly associated. As seen in Figure 4C, after addition of cysteamine to an AuMN-DTTC (0.15 mM Fe) suspension, the T2 relaxation time immediately decreased from 144.6 to 72.6 ms. This is expected as the cysteamine aggregates AuMN-DTTC through the gold nanoparticle component. As observed by absorbance measurements, after a certain threshold, large aggregates cannot stay in suspension and tend to precipitate. This was observed as an increase in the T2 relaxation time because, as the AuMN-DTTC precipitated, fewer nanoparticles remained in solution to generate a T2 effect. Further validation of our hypothesis was obtained by cysteamine treatment of an MN (0.15 mM Fe). We did not observe an effect on the T2 relaxation time of the solution, indicating that the corresponding change in the T2 relaxation time of AuMN-DTTC is the result of aggregation of the component gold nanostructures.

Finally, to confirm the aggregation of our probe upon thiol replacement, we monitored the particle size change of AuMN-DTTC with and without the addition of cysteamine. When we added cysteamine into a solution of AuMN-DTTC in water, we observed an immediate increase in particle size, which became more dramatic with time. These data further confirmed that the changes in the absorbance spectra and T2 relaxation times of the agent are due to aggregation of our probe by cysteamine treatment. Consistent with our earlier results, cysteamine treatment had no effect on the particle size of MN (Figure 4D).

Overall the relaxivity, UV−vis absorbance and particle size measurements suggest that AuMN-DTTC is stable in water, serum, and high-salt conditions, which is important for its application *in vivo*. The cysteamine treatment experiments indicate that the MN and AuNP components of our nanomaterial are strongly associated with each other.

***In silico* MRI and SERS Measurements on AuMN-DTTC.** After characterizating our probe and thoroughly investigating issues related to its stability, we focused our attention on evaluating the suitability of AuMN-DTTC as an MRI-SERS contrast agent. To that end, we first performed MRI on *in silico* phantoms comprising solutions in water of AuMN-DTTC and the control probes AuMN, AuNP, MN, and PBS. The iron content of MN, AuMN, and AuMN-DTTC was normalized to 0.45 mM prior to the scan, and the gold content of AuNP was normalized to AuMN-DTTC and AuMN (1.6 mM Au). As seen in the T2-weighted MR images (Figure 5A), the signal intensity of the AuMN-DTTC and AuMN solutions was comparable to MN and visibly lower than AuNP and PBS. This effect is consistent with the propensity for superparamagnetic iron oxides to shorten the transverse (T2) relaxation time of surrounding protons and reflects the capacity of our agent, like parental MN, to generate contrast on MR images. A quantitative assessment of T2 relaxation times was obtained using a multiecho MRI analysis. The T2 relaxation times of AuMN-DTTC, AuMN, and MN were 29.23 $\pm$ 1.45, 32.13 $\pm$ 3.26, and 31.58 $\pm$ 1.7 ms, respectively, whereas PBS and AuNP had T2 relaxation times of 783 $\pm$ 102 and 811 $\pm$ 75 ms, respectively, indicating that the latter solutions were nonmagnetic (Figure 5B). These data confirmed the validity of AuMN-DTTC as an MRI contrast agent.

After confirming that AuMN-DTTC has magnetic properties similar to MN, we analyzed the potential of our agent to also generate a SERS effect. To that end, we monitored the Raman spectra on AuMN-DTTC, AuMN, AuNP, and DTTC. We observed amplification of the efficiency of Raman scattering associated with AuMN-DTTC but not with any other controls. As we hypothesized, AuMN, which was designed as a SERS inactive material due to the absence of the DTTC Raman reporter on the gold surface, does not generate the Raman signature observed with AuMN-DTTC. The observed peaks in the SERS spectrum of AuMN-DTTC are very sharp, narrow, and clearly distinguished from the rest of the spectrum (Figure 5C). These findings demonstrate that AuMN-DTTC is not only useful as an MRI contrast agent but also has potential applications as a SERS-active imaging probe.

***In vivo* MRI and SERS Measurements of AuMN-DTTC.** The strong contrast-enhancing capabilities of AuMN-DTTC

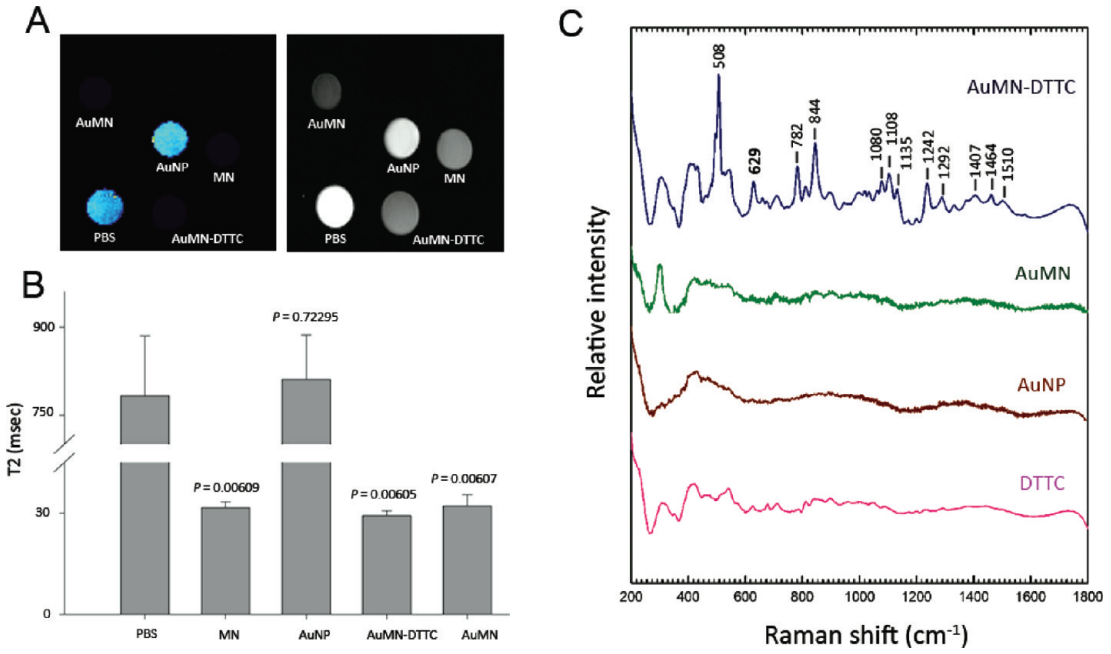

Figure 5. MRI and Raman spectroscopy *in silico*. A) T2-weighted MR image of AuMN-DTTC and the control probes in water. The signal intensities of AuMN-DTTC and AuMN were comparable to the intensity of the parental MN and noticeably lower than those of PBS and AuNP. (B) Calculated T2 values based on multiecho T2-weighted MRI. The T2 relaxation times of AuMN-DTTC and AuMN are comparable to the intensity of the parental MN and significantly lower than those of PBS and AuNP ($n = 3$; Student's t test; $p < 0.05$), indicating that the gold-doped probes are suitable as MRI contrast agents. (C) Raman spectra of AuMN-DTTC and control probes in water. AuMN-DTTC has a distinctive SERS signature, which is absent in the control probes.

demonstrated by our *in silico* studies suggested the possibility that this probe can also represent a suitable *in vivo* MRI-SERS contrast agent. To test this hypothesis, we first investigated whether we could obtain T2 contrast with our bimodal contrast agent in a living subject. To do so, we injected AuMN-DTTC and AuNP at equivalent gold concentrations in the right and left gluteal muscle, respectively, of female nude mice, as demonstrated in Figure 6A. After injection, we imaged the animals using a standard MRI multiecho T2-weighted protocol. The AuNP-injected area appeared bright, due to edema, which has a higher T2 value than surrounding muscle. By contrast, we observed a notable area of signal loss associated with the AuMN-DTTC injected area, which is an indication of contrast agent accumulation (Figure 6B). Quantitative analysis of tissue relaxation times at the injection sites revealed that the T2 value of noninjected muscle tissue was 33.4 $\pm$ 2.5 ms, whereas muscle tissue injected with AuMN-DTTC or AuNP had T2 relaxation times of 20.3 $\pm$ 2.2 and 157.4 $\pm$ 38.8 ms, respectively (Figure 6C).

Having established that AuMN-DTTC can generate excellent MRI contrast *in vivo*, we performed Raman spectroscopy to determine whether this probe can generate SERS signals. Measurements were performed prior to and following intramuscular probe injection in the live mouse. The mouse was placed on Raman spectroscopy platform and imaged by placing the Raman probe directly over the injected muscle, as shown in Figure 6D. AuMN-DTTC was injected in the right gluteal muscle, whereas AuMN, which is a SERS-inactive derivative of our probe, was injected in the left gluteal muscle. After the scan, the animal was sacrificed and the muscle tissue excised. The final data were analyzed by comparing the *in vivo* AuMN-DTTC spectra to those of AuMN-DTTC *in silico*, AuMN *in vivo*, and noninjected skin tissue. The results demonstrated a clear SERS observed both *in vivo* and *ex vivo*. It was also apparent that the SERS signatures obtained *in vivo* and *ex vivo* matched those gathered from AuMN-DTTC *in silico*. As seen in the Figure 6E, the marked SERS peaks in AuMN-DTTC *in silico* completely overlapped with the SERS peaks *in vivo* and in excised tissue. However the SERS effect was not observed in the skin nor the tissue injected with our MRI-active but SERS-inactive AuMN derivative. These findings assured us of the value of our probe not only to monitor biological events by MRI, an established *in vivo* imaging modality, but also to apply SERS in order to gather complementary information from the same environment.

Developing materials that can be used for clinical or preclinical *in vivo* imaging using multiple modalities has been a very active area of research in the imaging field. Confirming the presence of a disease-related abnormality with multiple imaging methods by using only one type of material will result in the rapid acquisition of reliable data, especially when one considers the increasing acceptance of multimodality instrumentation by the clinical and research communities. This type of data acquisition will also facilitate the

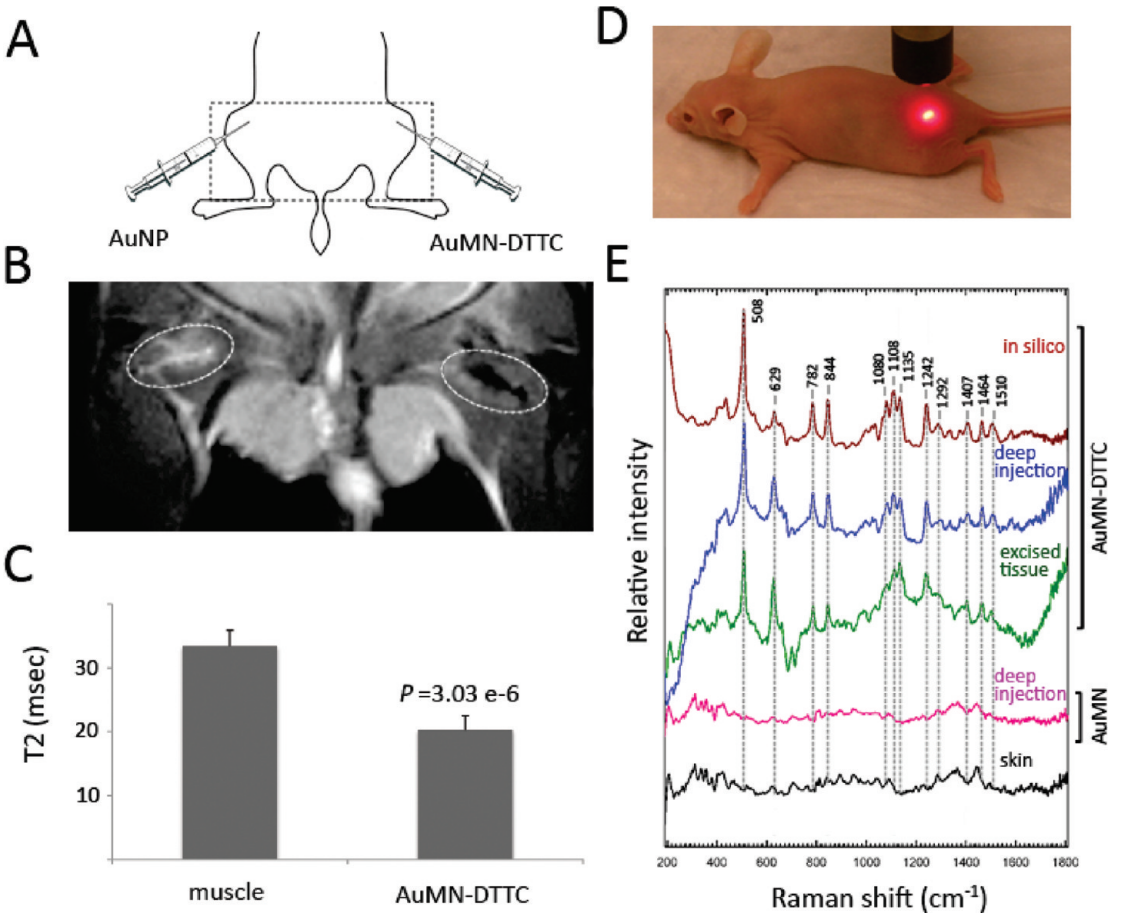

Figure 6. MRI and Raman spectroscopy *in vivo*. (A) A schematic of the probe injection setup. The experimental AuMN-DTTC probe was injected in the deep right gluteal muscle. A control probe was injected in the contralateral muscle. (B) *In vivo* T2-weighted MR image of a mouse injected intramuscularly (i.m.) with AuMN-DTTC and the control probe, AuNP. There is a notable loss of signal intensity associated with the site of the AuMN-DTTC injection, confirming the suitability of the probe as an *in vivo* MRI contrast agent. (C) Calculated T2 values based on multiecho T2-weighted MRI. The T2 relaxation time of AuMN-DTTC was significantly lower than both noninjected muscle and muscle injected with AuNP ($n = 3$; Student's t test; $p < 0.05$). (D) A photograph demonstrating the Raman spectroscopy experimental setup. E) *In vivo* Raman spectra of a mouse injected i.m. with AuMN-DTTC and the control probe, AuMN. The *in vivo* Raman spectrum of muscle injected with AuMN-DTTC has a clear SERS signature, which is indistinguishable from that obtained *ex vivo* and *in silico* and is absent in skin tissue and in muscle injected with the control probe.

collection of complementary information for a thorough characterization of biological phenomena. Here we report a novel nanoparticulate material with bimodal potential that can be imaged using magnetic resonance imaging and Raman spectroscopy. We demonstrate that the described probe is highly stable, biocompatible, and detectable using MRI and Raman spectroscopy by virtue of the SERS effect. This probe was fabricated without the use of bioincompatible chemicals during the synthesis process. Importantly, the probe can be visualized both *in silico* and *in vivo* in deep tissue in live animals. Considering the paucity of examples describing *in vivo* SERS-active probes and the importance of developing multimodal imaging strategies, we feel that the development of our agent is both timely and valuable as a new molecular imaging tool.

METHODS AND MATERIALS

Reagents. Gold(III) chloride hydrate, cysteamine, and hydroxylamine solutions were purchased from Aldrich (St Louis, MO). Sodium citrate tribasic dihyrate was purchased from Sigma (St Louis, MO), and 3,3′-diethylthiatricarbocyanine iodide (DTTC iodide) was purchased from Exciton (Dayton, OH). The mPEG-SH (MW ~5 kDa) was purchased from Laysan Bio, Inc. (Arab, AL). Fetal bovine serum was purchased from Atlanta Biologicals (Lawrenceville, GA). The chemicals were used as received from the corresponding vendors without further purification. MACS magnetic separation columns were purchased from Miltenyi Biotech (Auburn, CA).

Synthesis of the Bimodal MRI-SERS Contrast Agent (AuMN-DTTC). The synthesis of the MRI-SERS active nanomaterial (AuMN-DTTC) is schematically demonstrated in Figure 1A. Dextran-coated superparamagnetic iron oxide nanoparticles (MN) were synthesized according to the established protocol.[49] The MN was dialyzed against water and then concentrated to 9.2 mg/mL

(Fe/H_2O) using centricon concentrators with a 50 kDa cut off membrane. MN in water (600 μL) was mixed with 1332 μL of 1% (w/v) $HAuCl_4$ for 10 min. It is important to remove the sodium and citrate components from the MN solution during dialysis in order to avoid uncontrolled formation of gold clusters during $HAuCl_4$ and MN mixing. Following purification, 40 mL of 0.1% sodium citrate solution was heated to boiling in a round-bottom flask with strong uniform stirring. The MN and $HAuCl_4$ mixtures were added rapidly to the boiling 0.1% sodium citrate solution. The color of the solution turned red within five minutes, and the heat was removed. Once the solution was cooled to room temperature, the mixture was run through a MACS magnetic separation column and washed with ultrapure distilled water in order to remove nonmagnetic unassociated AuNP and excess sodium ions in the solution. The eluted red-colored suspension (10 mL) was incubated with 1300 μL 1% $HAuCl_4$ for 10 min in a 50 mL round-bottom flask with strong stirring at room temperature. To this mixture, 1800 μL of 100 mM NH_2OH was added dropwise. The color turned dark red, and 4000 μL of 100 μM DTTC in DMSO was subsequently added dropwise to the colloidal mixture with strong stirring. It is important to add the DTTC dropwise in order to avoid aggregation. After 10 min, 3000 μL of 5 kDa PEG-SH (1 mg/mL) was added dropwise to the suspension and stirred for 30 min. The resulting red-colored suspension was centrifuged for 10 min at 10 000 rpm in order to purify the contrast agent from free dye, PEG-SH, and MN. The red-colored nanoparticles precipitated, and unassociated MN was in the brown supernatant because free MNs do not precipitate by centrifugation at this speed. The precipitated particles were dispersed in 5 mL of ultrapure water and run though a magnetic column in order to remove unassociated gold nanostructures. The run-through eluted solution in the magnetic column was colorless, which indicates the absence of free AuNP in the suspension. The colloidal suspension retained in the magnetic column was dark red, suggesting that the AuNP were strongly associated with MNs and retained in the column. After washing the column with ultrapure water, the red suspension was eluted from the magnetic column by simply removing it from the magnetic column holder. This two-step purification was done three times in order to remove all the unassociated MNs and AuNPs. At the end of the third centrifugation, the supernatant was colorless, which indicated that there was no free MN in the suspension and that the remaining MNs in the precipitated pellet were associated with AuNP. The pellet was resuspended in 8 mL water. The final colloidal suspension was then filtered through a 0.22 μm syringe filter in order to remove large clusters. Almost no particulates were retained in the syringe filter, suggesting that the particles were small and dispersed in the solution but not aggregated. The resulting DTTC functionalized gold-doped iron oxide nanoparticles (AuMN-DTTC), (1.8 mM Fe, 7.0 mM Au) were characterized and redispersed in PBS buffer for animal studies. In order to synthesize the SERS inactive derivative of the probe (AuMN-DTTC), the DTTC addition step was skipped.

Synthesis of Gold Nanoparticles (AuNP). The gold nanoparticle suspension was prepared as follows: 20 mL of 1 mM $HAuCl_4$ was heated to boiling in a 50 mL round-bottom flask, and 2 mL of 1% sodium citrate solution was added rapidly into the boiling mixture. After the red color of AuNP was established, the burner was turned off, and the solution was stirred until cooled down to room temperature. Finally, the volume was adjusted to 20 mL.

Probe Characterization. The UV−vis absorbance measurements of AuMN-DTTC, AuMN (0.4 mM Fe, 1.5 mM Au), MN (0.4 mM Fe), and AuNP (1,5 mM Au) were performed at room temperature in a SpectraMax M2 (Molecular Devices, CA) spectrophotometer. The kinetic stability studies were performed using the same equipment. TEM was conducted on a JEOL JEM 200CX TEM at 200 kV. HRTEM/STEM/EDS were carried out on a JEOL JEM 2010F at 200 kV equipped with an INCA EDS system. Dynamic light-scattering measurements were performed using a Zetasizer Nano ZS (Malvern Instruments, MA) in triplicate. Intensity weighted values were used to determine the average particle diameter. Elemental analysis was done using inductively coupled plasma spectrometer (ICP) on AuNP, AuMN-DTTC, and MN in order to quantify the amount of gold and iron elements in the contrast agents. Iron content was determined using a standard iron assay protocol, as previously described.[49] *R*1 and *R*2 relaxivity measurements were performed using a Minispec mq20 NMR analyzer (Bruker, MA) and calculated by measuring the T1 and T2 parameters of the contrast agent solution at five different concentrations of Fe (0.32, 0.55, 0.78, 1.01, or 1.25 mM). In all of the studies, the gold content of the AuNPs was normalized to that of AuMN-DTTC by concentrating AuNPs *via* centrifugation until the plasmon resonance reading at 520 matched the 530 nm reading of AuMN-DTTC. The iron content of AuMN-DTTC was normalized to that of MN using iron assay.[49]

Stability Studies. The OD values of 1 mL of AuNP (0.15 mM Au) were recorded between 450 and 650 nm before and 20 min after the addition of 100 μL of 4 M NaCl and 10xPBS. Kinetic studies were performed by monitoring OD readings at 520 and 610 nm for 40 min.

For salt stability studies, the OD values of 1 mL AuMN-DTTC (0.15 mM Au) were recorded between 450 and 650 nm before and 20 min after the addition of 100 μL of 4 M NaCl and 10xPBS. For serum stability, the OD of fetal bovine serum was recorded as background, and the AuMN-DTTC stock solution was added into the serum to a final concentration of 0.15 mM Au. The spectra were obtained at 0 and 20 min after addition. For cysteamine-induced aggregation studies, 50 μL of 1 M of cysteamine was added into 1 mL of AuMN-DTTC solution. The absorbance spectrum was recorded before and 10 or 20 min after addition of cysteamine. Kinetic studies were performed by monitoring OD readings at 530 and 610 nm over 40 min.

For determining stability by magnetic relaxivity, the T2 values of 2 mL of AuMN-DTTC (0.15 mM Fe) were measured using a Minispec mq20 NMR analyzer (Bruker, MA) and calculated by measuring the T1 and T2 parameters of the contrast agent solution at five different concentrations of Fe (0.32, 0.55, 0.78, 1.01, or 1.25 mM). A 200 μL solution of 4 M NaCl and 10xPBS or 50 μL of 1 M cysteamine was added to 2 mL suspension after the fifth relaxivity reading. The T2 values of MN in 0.4 M NaCl and 1x PBS were performed in the same way. For serum stability, a stock solution of AuMN-DTTC was added to 2 mL of fetal bovine serum to a final concentration of 0.15 mM of iron and the T2 values monitored immediately after that.

The particle size measurements were performed by dynamic light scattering on 600 μL of AuMN-DTTC (0.1 mM Fe) and MN (0.1 mM Fe). Fifteen μL of 1 M cysteamine or 60 μL of 4 M NaCl and 10xPBS stock solution were added after the second reading.

MRI Measurements of Probe Phantoms. T2-weighted MR images of the AuMN-DTTC, AuMN (~0.45 mM Fe and 1.6 mM Au), MN (0.45 mM Fe), and AuNP (1.6 mM Au) were obtained using a 9.4T Bruker horizontal bore scanner (Billerica, MA) equipped with ParaVision 3.0 software. The imaging protocol consisted of coronal T2-weighted spin echo (SE) pulse sequences with the following parameters: SE TR/TE = 3000/ [8, 16, 24, 32, 40, 48, 56, 64]; FOV = 40 × 40 mm; matrix size = 128 × 128 pixels; slice thickness = 0.5 mm; and in-plane resolution = 312 × 312 μm^2. Image reconstruction and analysis were performed using Marevisi 3.5 software (Institute for Biodiagnostics, National Research Council, Canada). T2 maps were constructed according to the established protocol by fitting the T2 values for each of the eight echo times (TE) to a standard exponential decay curve. T2 relaxation times were calculated by manually segmenting out the probe solutions on MR images.

SERS Measurements of Probe Phantoms. The Raman spectra were obtained using a commercial portable Raman unit (Aspire, Raman System Inc.). In this system, laser light from a diode laser is fiber-coupled to a flexible probe head. The probe head focuses the laser beam on the sample for Raman excitation. The focused beam spot diameter is around 50 μm. The excitation light wavelength is 785 nm, and the laser power at the sampling position is 250 mW. The Raman scattering light is collected using the same probe head. The collected Raman light is separated from the excitation light by a dichroic mirror and fiber delivered to a monochromator. The resolution of the spectrometer is around 6 cm^{-1}. The readings were performed on 4 mL of AuMN-DTTC, AuMN, AuNP (7 mM Au), and 2 μM DTTC with a 5 s integration time.

Animals. Six week old female nude mice (Massachusetts General Hospital Radiation Oncology breeding facilities; $n = 8$) were used in our MRI-SERS experiments. All animal experiments were performed in compliance with institutional guidelines and approved by the Subcommittee on Research Animal Care (SRAC) at Massachusetts General Hospital.

Animal MRI Studies. Six week old female nude mice were injected with 50 μL AuMN-DTTC (Fe, 2.5 mg/kg, 70 mM Au) in the right gluteal muscle. The left gluteal muscle was injected with 50 μL AuNPs (70 mM Au) (Figure 5A). T2-weighted MR images were obtained using the same instrumentation and scan protocols as described for the *in silico* studies. T2 relaxation times were calculated by manually segmenting out the injected tissue on MR images.

Animal SERS Studies. Imaging was performed before and after injection with 50 μL of AuMN-DTTC (Fe (2.5 mg/kg), 70 mM Au) in the right gluteal muscle. The left gluteal muscle was injected with 50 μL of AuMN [Fe (2.5 mg/kg), 70 mM Au]. Raman spectrometer used was the Raman Systems model Aspire-785 L with 785 nm laser excitation. The area to be injected was marked prior to injection. The SERS spectra were obtained as described for the *in silico* studies by performing measurements with a 60 s integration time. After the *in vivo* SERS, the mice were sacrificed, and the injected tissues excised. SERS spectra of the excised muscle tissue were obtained using the same parameters as the *in vivo* studies.

Statistical Analysis. Data were expressed as mean $\pm$ standard deviation (SD). Statistical differences were analyzed by the Student's t test (SigmaStat 3.0; Systat Software, Richmond, CA). A value of $P < 0.05$ was taken as statistically significant.

Acknowledgment. We thank P. Pantazopoulos (Martinos Center for Biomedical Imaging, MGH) for help with the *in silico* assays, R. Uppal and P. Caravan (Martinos Center for Biomedical Imaging, MGH) for help with ICP-MS, and R. M. Papaleo for his helpful discussions on TEM images. Work at the Martinos Center for Biomedical Imaging was supported under grant R00CA129070 from the National Cancer Institute. TEM work made use of the MIT EM shared facilities of the Material Research Science and Engineering Center (MRSEC) supported by NSF.

Supporting Information Available: Additional analyses of AuMN-DTTC including HR-TEM images, STEM/EDS elemenatal maps, DLS and systematic toxicity. This material is available free of charge *via* the Internet at http://pubs.acs.org.

REFERENCES AND NOTES

1. Bulte, J. W. M.; Kraitchman, D. L. Iron Oxide MR Contrast Agents for Molecular and Cellular Imaging. *NMR Biomed.* **2004,** *17*, 484–499.
2. Alivisatos, P. The Use of Nanocrystals in Biological Detection. *Nat. Biotechnol.* **2004,** *22*, 47–52.
3. Ferrari, M. Cancer Nanotechnology: Opportunities and Challenges. *Nat. Rev. Cancer* **2005,** *5*, 161–171.
4. Niemeyer, C. M. Nanoparticles, Proteins, and Nucleic Acids: Biotechnology Meets Materials Science. *Angew. Chem., Int. Ed.* **2001,** *40*, 4128–4158.
5. Yigit, M. V.; Mazumdar, D.; Kim, H. K.; Lee, J. H.; Odintsov, B.; Lu, Y. Smart "Turn-On" Magnetic Resonance Contrast Agents Based on Aptamer-Functionalized Superparamagnetic Iron Oxide Nanoparticles. *ChemBioChem* **2007,** *8*, 1675–1678.
6. Medarova, Z.; Pham, W.; Farrar, C.; Petkova, V.; Moore, A. *In-Vivo* Imaging of SiRNA Delivery and Silencing in Tumors. *Nat. Med.* **2007,** *13*, 372–377.
7. Sun, C.; Fang, C.; Stephen, Z.; Veiseh, O.; Hansen, S.; Lee, D.; Ellenbogen, R. G.; Olson, J.; Zhang, M. Tumor-Targeted Drug Delivery and MRI Contrast Enhancement by Chlorotoxin-Conjugated Iron Oxide Nanoparticles. *Nanomedicine* **2008,** *3*, 495–505.
8. Shi, M.; Ho, K.; Keating, A.; Shoichet, M. S. Doxorubicin-Conjugated Immuno-Nanoparticles for Intracellular Anticancer Drug Delivery. *Adv. Funct. Mater.* **2009,** *19*, 1689–1696.
9. Liu, J.; Lu, Y. Fast Colorimetric Sensing of Adenosine and Cocaine Based on a General Sensor Design Involving Aptamers and Nanoparticles. *Angew. Chem., Int. Ed.* **2006,** *45*, 90–94.
10. Josephson, L.; Perez, J. M.; Weissleder, R. Magnetic Nanosensors for the Detection of Oligonucleotide Sequences. *Angew. Chem., Int. Ed.* **2001,** *40*, 3204–3206.
11. Patra, C. R.; Bhattacharya, R.; Mukhopadhyay, D.; Mukherjee, P. Fabrication of Gold Nanoparticles for Targeted Therapy in Pancreatic Cancer. *Adv. Drug Delivery Rev.* **2009**.
12. Peer, D.; Karp, J. M.; Hong, S.; Farokhzad, O. C.; Margalit, R.; Langer, R. Nanocarriers as an Emerging Platform for Cancer Therapy. *Nat. Nanotechnol.* **2007,** *2*, 751–760.
13. Boisselier, E.; Astruc, D. Gold Nanoparticles in Nanomedicine: Preparations, Imaging, Diagnostics, Therapies and Toxicity. *Chem. Soc. Rev. 38*, 1759-1782.
14. Berry, C. C.; Curtis, A. S. G. Functionalisation of Magnetic Nanoparticles for Applications in Biomedicine. *J. Phys. D: Appl. Phys.* **2003,** *36*, R198–R206.
15. Sanles-Sobrido, M.; Exner, W.; Rodríguez-Lorenzo, L.; Rodríguez-González, B.; Correa-Duarte, M. A.; Álvarez-Puebla, R. A.; Liz-Marzán, L. M. Design of SERS-Encoded, Submicron, Hollow Particles Through Confined Growth of Encapsulated Metal Nanoparticles. *J. Am. Chem. Soc.* **2009,** *131*, 2699–2705.
16. Kim, K.; Choi, J.-Y.; Lee, H. B.; Shin, K. S. Silanization of Ag-Deposited Magnetite Particles: An Efficient Route to Fabricate Magnetic Nanoparticle-Based Raman Barcode Materials. *ACS Appl. Mater. Interfaces* **2010,** *2*, 1872–1878.
17. Spuch-Calvar, M.; Rodríguez-Lorenzo, L.; Morales, M. P.; Álvarez-Puebla, R. A.; Liz-Marzán, L. M. Bifunctional Nanocomposites with Long-Term Stability as SERS Optical Accumulators for Ultrasensitive Analysis. *J. Phys. Chem. C* **2008,** *113*, 3373–3377.
18. Bouchard, L. S.; Anwar, M. S.; Liu, G. L.; Hann, B.; Xie, Z. H.; Gray, J. W.; Wang, X.; Pines, A.; Chen, F. F. Picomolar Sensitivity MRI and Photoacoustic Imaging of Cobalt Nanoparticles. *Proc. Natl. Acad. Sci. U.S.A.* **2009,** *106*, 4085–9.
19. Xu, Z.; Hou, Y.; Sun, S. Magnetic Core/Shell Fe3O4/Au and Fe3O4/Au/Ag Nanoparticles with Tunable Plasmonic Properties. *J. Am. Chem. Soc.* **2007,** *129*, 8698–8699.
20. Glaus, C.; Rossin, R.; Welch, M. J.; Bao, G. *In Vivo* Evaluation of 64Cu-Labeled Magnetic Nanoparticles as a Dual-Modality PET/MR Imaging Agent. *Bioconjugate Chem.* **2010,** *21*, 715–722.
21. Xie, J.; Chen, K.; Huang, J.; Lee, S.; Wang, J.; Gao, J.; Li, X.; Chen, X. PET/NIRF/MRI Triple Functional Iron Oxide Nanoparticles. *Biomaterials* **2010,** *31*, 3016–3022.
22. Harisinghani, M. G.; Barentsz, J.; Hahn, P. F.; Deserno, W. M.; Tabatabaei, S.; van de Kaa, C. H.; de la, R. J.; Weissleder, R. Noninvasive Detection of Clinically Occult Lymph-Node Metastases in Prostate Cancer. *N. Engl. J. Med.* **2003,** *348*, 2491–2499.
23. Connor, E. E.; Mwamuka, J.; Gole, A.; Murphy, C. J.; Wyatt, M. D. Gold Nanoparticles are Taken Up by Human Cells but Do Not Cause Acute Cytotoxicity. *Small* **2005,** *1*, 325–327.
24. Merchant, B. Gold, The Noble Metal and The Paradoxes of Its Toxicology. *Biologicals* **1998,** *26*, 49–59.
25. Root, S. W.; Andrews, G. A.; Kniseley, R. M.; Tyor, M. P. The Distribution and Radiation Effects of Intravenously Administered Colloidal Gold-198 in Man. *Cancer* **1954,** *7*, 856–866.
26. Sun, I. C.; Eun, D. K.; Na, J. H.; Lee, S.; Kim, I. J.; Youn, I. C.; Ko, C. Y.; Kim, H. S.; Lim, D.; Choi, K.; et al. Heparin-Coated Gold Nanoparticles for Liver-Specific CT Imaging. *Chemistry* **2009,** *15*, 13341–7.
27. Popovtzer, R.; Agrawal, A.; Kotov, N. A.; Popovtzer, A.; Balter, J.; Carey, T. E.; Kopelman, R. Targeted Gold Nanoparticles Enable Molecular CT Imaging of Cancer. *Nano Lett.* **2008,** *8*, 4593–6.
28. Liu, J.; Lu, Y. A Colorimetric Lead Biosensor Using DNAzyme-Directed Assembly of Gold Nanoparticles. *J. Am. Chem. Soc.* **2003,** *125*, 6642–6643.
29. Liu, J.; Lu, Y. Adenosine-Dependent Assembly of Aptazyme-Functionalized Gold Nanoparticles and Its

Application as a Colorimetric Biosensor. *Anal. Chem.* **2004,** *76*, 1627–1632.
30. Evgenov, N. V.; Medarova, Z.; Dai, G.; Bonner-Weir, S.; Moore, A. *In Vivo* Imaging of Islet Transplantation. *Nat. Med.* **2006,** *12*, 144–8.
31. Medarova, Z.; Rashkovetsky, L.; Pantazopoulos, P.; Moore, A. Multiparametric Monitoring of Tumor Response to Chemotherapy by Noninvasive Imaging. *Cancer Res.* **2009,** *69*, 1182–9.
32. Sosnovik, D. E.; Weissleder, R. Emerging Concepts in Molecular MRI. *Curr. Opin. Biotechnol.* **2007,** *18*, 4–10.
33. Doering, W. E.; Nie, S. M. Spectroscopic Tags Using Dye-Embedded Nanoparticles and Surface-Enhanced Raman Scattering. *Anal. Chem.* **2003,** *75*, 6171–6176.
34. Kneipp, K. Single Molecule Detection Using Surface Enhanced Raman Scattering. *Phys. Rev. Lett.* **1997,** *78*, 1667–1670.
35. Michaels, A. M.; Nirmal, M.; Brus, L. E. Surface Enhanced Raman Spectroscopy of Individual Rhodamine 6G Molecules on Large Ag Nanocrystals. *J. Am. Chem. Soc.* **1999,** *121*, 9932–9939.
36. Qian, X.; Peng, X. H.; Ansari, D. O.; Yin-Goen, Q.; Chen, G. Z.; Shin, D. M.; Yang, L.; Young, A. N.; Wang, M. D.; Nie, S. *In Vivo* Tumor Targeting and Spectroscopic Detection with Surface-Enhanced Raman Nanoparticle Tags. *Nat. Biotechnol.* **2008,** *26*, 83–90.
37. Campion, A.; Kambhampati, P. Surface-Enhanced Raman Scattering. *Chem. Soc. Rev.* **1998,** *27*, 241–250.
38. Moore, B. D. Rapid and Ultra-Sensitive Determination of Enzyme Activities Using Surface-Enhanced Resonance Raman Scattering. *Nat. Biotechnol.* **2004,** *22*, 1133–1138.
39. Nie, S. M.; Emory, S. R. Probing Single Molecules and Single Nanoparticles by Surface-Enhanced Raman Scattering. *Science* **1997,** *275*, 1102–1106.
40. Kneipp, K.; Kneipp, H.; Itzkan, I.; Dasari, R. R.; Feld, M. S. Ultrasensitive Chemical Analysis by Raman Spectroscopy. *Chem. Rev.* **1999,** *99*, 2957–2976.
41. Stoeva, S. I.; Huo, F.; Lee, J. S.; Mirkin, C. A. Three-Layer Composite Magnetic Nanoparticle Probes for DNA. *J. Am. Chem. Soc.* **2005,** *127*, 15362–3.
42. Panyam, J.; Labhasetwar, V. Biodegradable Nanoparticles for Drug and Gene Delivery to Cells and Tissue. *Adv. Drug Delivery Rev.* **2003,** *55*, 329–347.
43. Mirkin, C. A.; Letsinger, R. L.; Mucic, R. C.; Storhoff, J. J. A DNA-Based Method for Rationally Assembling Nanoparticles Into Macroscopic Materials. *Nature* **1996,** *382*, 607–609.
44. Storhoff, J. J.; Elghanian, R.; Mucic, R. C.; Mirkin, C. A.; Letsinger, R. L. One-Pot Colorimetric Differentiation of Polynucleotides with Single Base Imperfections Using Gold Nanoparticle Probes. *J. Am. Chem. Soc.* **1998,** *120*, 1959–1964.
45. Perez, J. M.; Josephson, L.; O'Loughlin, T.; Hoegemann, D.; Weissleder, R. Magnetic Relaxation Switches Capable of Sensing Molecular Interactions. *Nat. Biotechnol.* **2002,** *20*, 816–820.
46. Perez, J. M.; O'Loughin, T.; Simeone, F. J.; Weissleder, R.; Josephson, L. DNA-Based Magnetic Nanoparticle Assembly Acts as a Magnetic Relaxation Nanoswitch Allowing Screening of DNA-Cleaving Agents. *J. Am. Chem. Soc.* **2002,** *124*, 2856–2857.
47. Tsourkas, A.; Hofstetter, O.; Hofstetter, H.; Weissleder, R.; Josephson, L. Magnetic Relaxation Switch Immunosensors Detect Enantiomeric Impurities. *Angew. Chem., Int. Ed.* **2004,** *43*, 2395–2399.
48. Yigit, M. V.; Mazumdar, D.; Lu, Y. MRI Detection of Thrombin with Aptamer Functionalized Superparamagnetic Iron Oxide Nanoparticles. *Bioconjugate Chem.* **2008,** *19*, 412–417.
49. Medarova, Z.; Evgenov, N. V.; Dai, G.; Bonner-Weir, S.; Moore, A. *In Vivo* Multimodal Imaging of Transplanted Pancreatic Islets. *Nat. Protocols* **2006,** *1*, 429–435.